Quantifying Structural Heterogeneity in Individual $CsPbBr_3$ Quantum Dot Superlattices

Daniel E. Clark,[1] Victoria A. Lumsargis,[1] Daria D. Blach,[1] Kuixin Zhu,[1] Alexander J. Shumski,[1] Lehan Yao,[2] Qian Chen,[2] Libai Huang,*[1] Christina W. Li*[1]

[1] Department of Chemistry, Purdue University, West Lafayette, Indiana 47907, USA.

[2] Department of Materials Science and Engineering, University of Illinois, Urbana, Illinois 61801, USA.

Supporting Information Placeholder

ABSTRACT: A thorough understanding of structural heterogeneity in $CsPbBr_3$ quantum dot superlattices (SLs) is necessary for the realization of exciton coherence in these systems. Scanning transmission electron microscopy (STEM) coupled to fast-Fourier transform (FFT) analysis is utilized to characterize the structural properties of individual SLs. For each SL, the average constituent quantum dot size, size dispersity, and number of crystalline domains are quantified. Analysis of 40 individual SLs across eight growth experiments reveal that SLs are structurally heterogeneous but tend to have a narrower size distribution than the precursor solution due to size selection that occurs during evaporative self-assembly. We directly correlate STEM-FFT structural properties to low-temperature photoluminescence spectra for individual SLs, demonstrating that substructure in the photoluminescence peak arises from multiple, locally-ordered domains within the SL. In addition, we show that long-range structural disorder in a SL does not necessarily impact short-range phenomena such as exciton delocalization.

Ordered superlattices (SLs) grown from $CsPbBr_3$ quantum dots (QDs) have attracted a great deal of attention because of the observation of coupled photoemission behavior, superfluorescence or superradiance, at low temperature.[1-6] These 3D SLs self-assemble from a colloidal solution of cubic QDs as the solvent evaporates, ranging widely in macroscopic size, shape, and aspect ratio.[2,7-15] Identifying and quantifying these forms of SL structural heterogeneity will be critical toward understanding how exciton delocalization competes with disorder in $CsPbBr_3$ 3D SLs. In Rainò et al.'s work, superfluorescence from up to 28 coupled QDs was observed at 6 K at high excitation fluence because of coherence induced by photoexcitation.[1] More recently, our group showed that $CsPbBr_3$ cubic SLs also exhibit single-photon superradiance arising from exciton delocalization at low excitation fluence. Unlike superfluorescence, superradiance does not require a light-induced phase-synchronization of emitters.[16] However, we found that the number of coherent emitters in the superradiant state varied widely across SLs grown under the same conditions, which was reflected in their heterogeneous photoluminescence (PL) spectra and lifetimes at low temperature. Dynamic disorder from phonon scattering becomes negligible at 11 K, which indicates that differences in PL properties stem strictly from structural heterogeneity among SLs.[3,17] SL structural heterogeneity can exist in many forms including size-based segregation of the constituent QDs into separate SLs (**Scheme 1a**), a broad size distribution of QDs in a single SL (**Scheme 1b**), disordered packing at SL surfaces (**Scheme 1c**), and misaligned domains (**Scheme 1d**).

Scheme 1. Types of SL structural disorder possible in self-assembled structures.

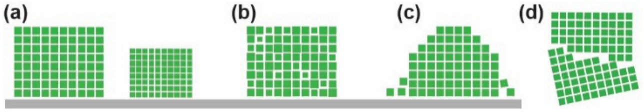

The self-assembly and structural properties of $CsPbBr_3$ SLs have been studied in the literature through X-ray scattering and diffraction techniques, which interrogate the average properties of many SLs in a solution or powder sample.[8,12,18-21] Samples containing highly-ordered SLs exhibit sharp small-angle and wide-angle X-ray scattering features due to the long-range ordering of QDs within the SLs. The average center-to-center distance between QDs can be extracted from the peak position, and the average domain size can be estimated from peak broadening. However, in a non-uniform SL sample such as those prepared from evaporative self-assembly, these average methods are insufficient to structurally explain the diverse PL properties we observe for individual SLs. Lapkin et al. utilized spatially-resolved X-ray diffraction, scattering, and PL to map the structural and optical heterogeneity within a single SL.[22] The authors observed significant compressive strain and structural disorder at the edge of the SL, which were correlated to a blue-shift and shorter lifetime in the PL. However, structural and optical heterogeneity across different SLs were not probed in this work. To understand the SL structural properties that lead to coherence, we aim to quantify the structural parameters of many individual SLs prepared under identical growth conditions using fast-Fourier transform (FFT) analysis of high-angle annular dark-field scanning transmission electron microscopy (HAADF-STEM) images and perform one-to-one correlations to their low-temperature PL properties.

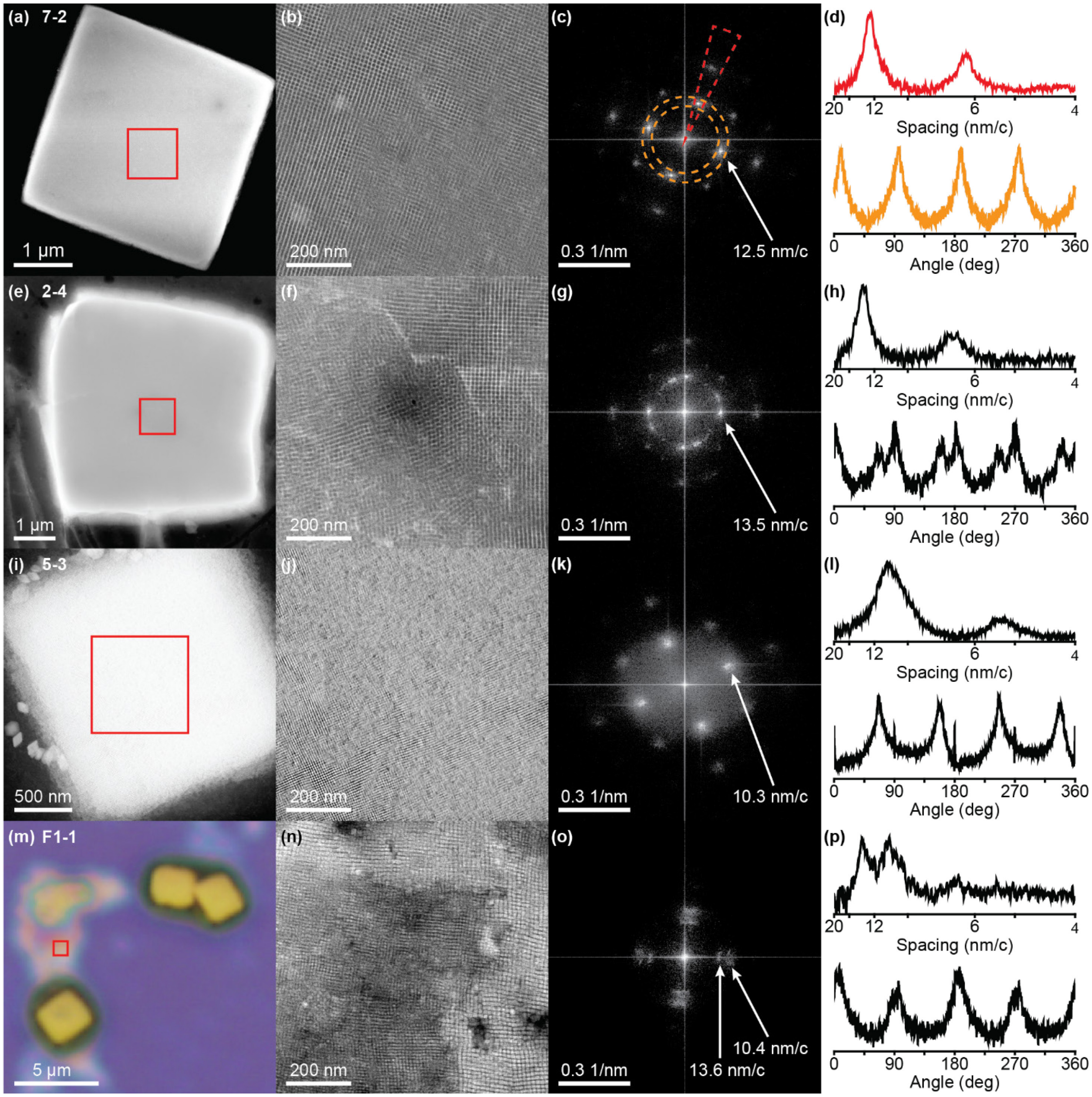

Figure 1. STEM imaging and FFT structural analysis for three representative $CsPbBr_3$ SLs (7-2, 2-4, and 5-3) and one film (F1-1). Included for each sample is the low-resolution image, zoomed-in HAADF-STEM image, corresponding FFT pattern, and extracted radial and angular FFT data.

Quantifying Superlattice Order through STEM-FFT

To quantify the structural heterogeneity observed in a population of $CsPbBr_3$ SLs, HAADF-STEM images were collected for 40 individual SLs across eight samples (**Figure 1, S1-S2)**. These SLs were grown directly on TEM grids via evaporation of a colloidal solution of $CsPbBr_3$ cubic QDs (details in SI section 2). SLs are labeled #-# where the first number indicates the sample and the second indicates the individual SL on that sample. All images are obtained using dark-field STEM, but we observe a thickness-dependent contrast change that does not influence the structural analysis (details in SI section 5).

We then performed FFT analysis of an 836 by 836 nm^2 image centered on the SL to obtain a more quantitative representation of the periodic order within the STEM image (**Figure 1b**). The FFT extracts the frequency (1/nm) and angle of the ordered rows of QDs and plots them in polar coordinates along the radial and angular axes, respectively (**Figure 1c**). The radial position of the FFT spots, converted to a 2D plot in Figure 1d by extracting the data in the red wedge, is representative of the average spacing of the QD rows and columns within the SL (**Figure 1c, d**). The angle at which each FFT spot occurs can be obtained from the data in the yellow ring, which represents the orientation of the SL domain(s).

All $CsPbBr_3$ SLs exhibit simple cubic crystal packing based on the presence of four angular peaks spaced at 90° intervals (**Figure 1d**). In the radial profile, the position of the strongest peak represents the primary QD center-to-center (CtC) spacing in the cubic arrangement. A weaker peak at half of the primary spacing also appears, a feature which arises only in highly periodic images. Differences in radial peak position from one SL to another arise from changes in the constituent QD size since the capping ligands occupy the same amount of space in all cases (**Figure S3**). Concurrently, the full-width at half-maximum (FWHM) of the major radial peak can be used to approximate the size distribution of QDs within each SL (**Table S1**).

Figure 1 illustrates the structural and morphological heterogeneity observed in our self-assembled SL samples. SL 7-2 (**Figure 1a-d**) exhibits one simple cubic domain with radial peak position of 12.45 ± 0.11 nm and radial FWHM of 2.06 ± 0.21 nm, making it one of the more ordered SLs within the population. SL 2-4 (**Figure 1e-h**), while exhibiting a similar CtC spacing and FWHM, contains multiple crystalline domains based on the presence of multiple sets of four angular spots in the FFT, which may contribute to its more distorted macroscopic shape. SL 5-3 (**Figure 1i-l**), substantially smaller and thinner in macroscopic size compared to the previous two SLs, shows a smaller CtC spacing of 10.32 ± 0.03 nm and larger radial FWHM of 3.13 ± 0.35 nm. All samples also contain a significant amount of dense QD film material in the vicinity of the SLs that show modest ordering in the STEM image (**Figure 1m-n, S4 and Table S2**). These film regions still show simple cubic packing of QDs but are multimodal or broadened in their radial and angular FFT peaks due to the wide distribution of QD sizes and orientations present (**Figure 1o-p**). On average, the radial peak center and FWHM in five dense QD film regions is 10.9 ± 0.6 nm and 4.6 ± 0.7 nm, respectively. These films represent the population of QDs that remain unincorporated after the SL growth terminates.

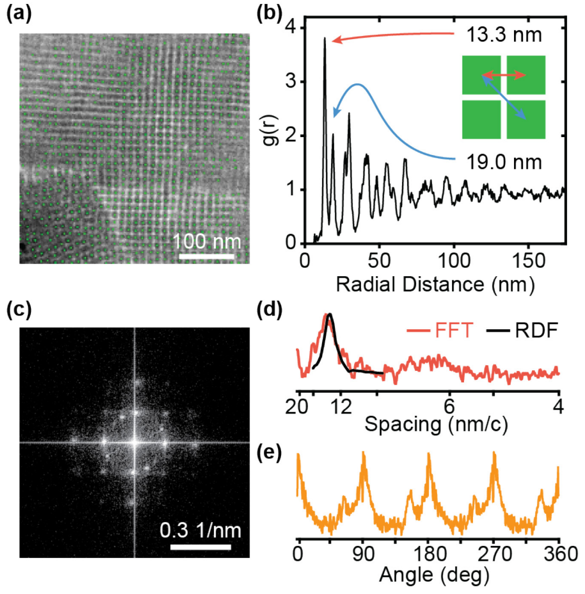

Figure 2. **(a)** STEM image of a SL with QD centroids indicated in green, **(b)** radial distribution function generated from STEM image, **(c)** FFT pattern of same region, **(d)** extracted radial, and **(e)** angular data from FFT.

As a validation of our method, FFT analysis was performed on a simulated image of perfectly aligned 10.02 nm cubes with 3.15 nm inter-cube spacing (**Figure S5**). The radial peak position from the FFT analysis (13.34 nm) matches closely to the actual CtC spacing (13.17 nm). However, the radial FWHM was substantially larger than zero despite the perfect periodicity in this image, indicating that a major component of the radial peak broadening is inherent to the fast Fourier transform (**Table S3**).[23] We also compared the STEM-FFT analysis to a radial distribution function (RDF) generated by directly locating QD centroids within the STEM image (**Figure 2a**).[24,25] The RDF analysis is carried out on a smaller image than our typical FFT analysis because centroid locations can only be accurately determined in regions of high order. The first peak in the RDF at 13.30 nm measures the distance between nearest neighbor QD centers, and the FWHM of 1.75 nm reflects positional disorder in the QD centers (**Figure 2b**). The subsequent peaks in the RDF are indicative of a simple cubic arrangement of QDs, and long-range order persists over the length scale of the entire image.[26] The radial FFT fitting of the same region gives consistent results: a CtC distance of 13.51 nm and FWHM of 2.66 nm (**Figure 2c-d**). The angular FFT data reveals a more significant difference between the two analyses. Because RDF relies on QD center position without considering orientation, the presence of a rotated second crystal domain in the bottom left corner of Figure 2a is not captured. In contrast, the angular slice of the FFT pattern in Figure 2c shows that two sets of peaks are present, and the relative intensity of the two peak sets corresponds to the relative area of each domain in the STEM image (**Figure 2e**). In our view, the primary advantage of the STEM-FFT analysis is that it can be performed on all SL and dense film STEM images regardless of their degree of ordering and number of domains (**Figure S6**), enabling characterization of a broad distribution of structurally heterogeneous samples.

Superlattice Structural Trends

To understand structural trends within the SL population, we constructed histograms for the FFT radial peak center and FWHM for all 40 SLs (**Figure 3a-b**). The SLs exhibit a broad range of radial peak broadening, but over 90% have a FWHM narrower than the 4.6 nm observed on average in the dense QD films (**Figure 3a**). The observation that SLs are considerably more monodisperse than the surrounding film suggests that size-selection occurs during the evaporative self-assembly process. The radial FFT peak position, representative of the QD CtC distance in each SL, also ranges widely from 9 to 15 nm in the population with a slight skew toward larger QD sizes (**Figure 3b**). In comparison, the dense films exhibit an average CtC spacing of 10.9 nm, similar to the average QD size in the precursor solution (8.1 ± 1.8 nm) assuming a constant 3.0 nm ligand gap length (**Figure S3**). The variation in CtC spacing combined with the narrow FWHM values corroborates the hypothesis that QDs of similar size tend to spontaneously self-assemble. Together, these data show that the solvent evaporation self-assembly method grows $CsPbBr_3$ SLs with larger average QD size and narrower size distribution than the colloidal solution from which they were derived.

We also correlated the FFT parameters to macroscopic properties of the SL, including its edge length and height. Under our growth conditions, we observe SLs ranging in edge length from 1.0 to 5.5 μm (**Table S1**). While SLs may appear cubic in the 2D projections, tilted SEM images reveal that all SLs have a smaller height dimension than edge length (**Figure S7**). SLs range in height from 50 nm to 2 μm with the largest height to edge ratios reaching ~0.5. We find that SL height is the macroscopic property most closely correlated to FFT structural parameters (**Figure 3c, S8**). When the SL contains a polydisperse distribution of QD sizes, characterized by radial FWHM > 4 nm, SLs are never able to grow beyond 1 μm in height regardless of the average QD sizes present (**Figure 3c, circled**). In the more ordered SLs, a range of heights are observed but are discriminated by their constituent QD sizes. SLs comprising small QDs (FFT center <11 nm) are all <1 μm in height while SLs containing larger QDs can grow up to 2 μm thick.

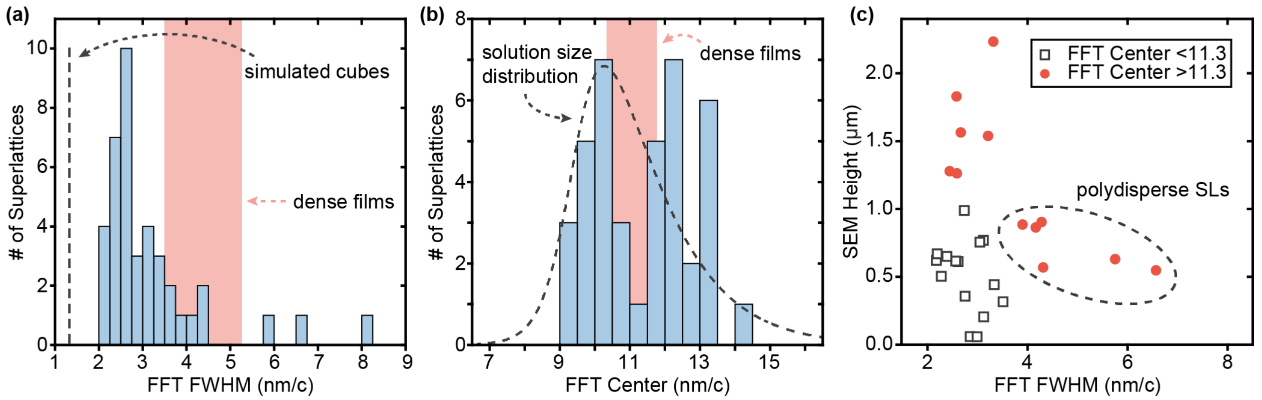

Figure 3. Histograms of FFT structural properties for a population of 40 SLs: **(a)** radial FWHM and **(b)** radial peak center (the solution size distribution has a 3.0 nm ligand gap added for comparison). **(c)** SL height vs. FFT linewidth.

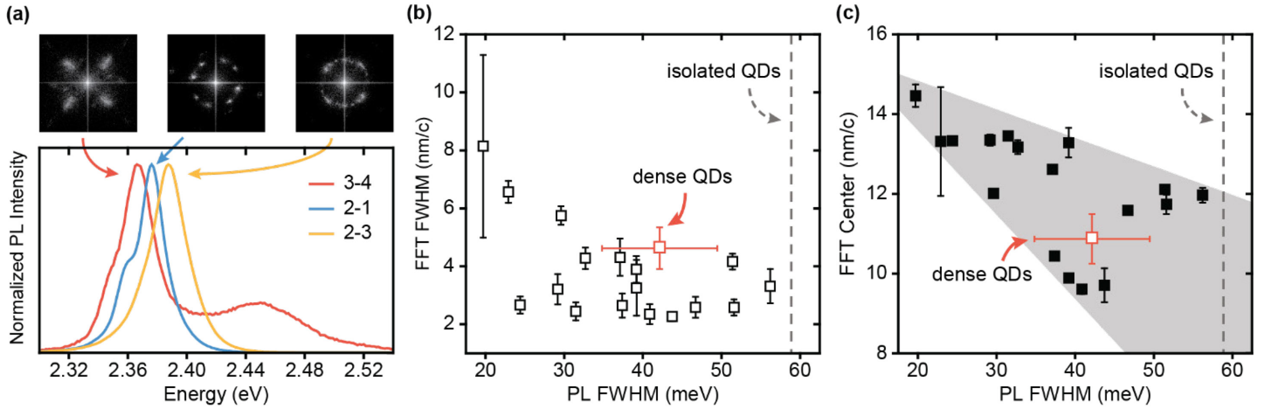

Figure 4. **(a)** Low-temperature PL spectra and FFT patterns for multi-domain SLs. Correlation between 7 K PL linewidth and (**b**) FFT linewidth or (**c**) FFT peak center.

These SL structural trends are congruent with previous studies on SL growth dynamics during evaporative self-assembly using other nanocrystal cores.[27,28] Many factors are known to influence nanocrystal assembly dynamics in solution, including size, shape and faceting, ligand density, concentration, and solubility.[29-35] Among these factors, the starting nanocrystal size likely plays an important role in our $CsPbBr_3$ SL assemblies because the other factors remain constant in a single growth experiment. Several studies utilizing in-situ X-ray scattering and theoretical modeling have elucidated how nanocrystal size impact attractive (van der Waal's) and repulsive (ligand sterics, osmotic pressure) interactions between individual nanocrystals in SL growth.[36-38] These studies show that larger nanocrystals begin to assemble into ordered SLs at earlier time points and lower solution concentration than smaller nanocrystals due to their stronger attractive interactions. The final morphology and degree of ordering, however, depend upon the composition and morphology of the constituent nanocrystals and the specific conditions of the growth experiment.

In a study on Fe_2O_3 cubes capped with oleic acid, larger nanocubes (9.1 nm) formed cuboidal mesocrystals in the 1-3 um size regime with simple cubic packing, similar to those observed in our $CsPbBr_3$ growths. [36] Smaller nanocubes (6.8 nm) formed spherical superstructures with a mixture of simple cubic and face-centered cubic crystal structures. Monodisperse PbS and Au nanospheres have also shown size-dependent SL morphology, crystal packing, and defect density.[39,40] All of these examples were grown from colloidal solutions with <10% size dispersity, which facilitates crystalline SL assembly.[41,42] In an example of CdSe SLs grown from a more polydisperse colloidal solution, nanocrystal size selection was observed during evaporative self-assembly.[43] Both the TEM and PL data confirmed that SLs comprised a narrower size distribution than the precursor colloidal solution while amorphous films on the same samples showed broader and more red-shifted PL peaks due to their larger nanocrystal size distribution.

Correlating Superlattice Structure to Optical Properties

To examine if SL structural properties influence their exciton delocalization and coherence, low temperature PL (7 K) was collected for 17 of the $CsPbBr_3$ SLs (**Figure S2, 9a**). A beam diameter of 910 nm was used for all PL measurements, and the excitation wavelength at 447 nm has a penetration depth of ~400 nm. The lateral extent of the optical probe is comparable in size to the STEM images, but the penetration depth is significantly lower for tall (>500 nm height) SLs. Surface disorder as well as structural heterogeneity in the vertical and lateral dimensions may convolute direct correlations between PL and STEM-FFT properties (see SI section 4-5).

The first question we asked was whether substructure in the low-temperature PL spectrum arises from multiple, locally-ordered domains in the SL. In our SL population, the most complex PL spectra show three features, for example in SL 3-4 (**Figure 4a**, red). The broad, high energy feature at 2.450 eV arises from uncoupled QDs in the vicinity of the SLs, matching closely in energy and FWHM to a film of dilute QDs embedded in a polymer matrix (**Figure S9c**). The red-shifted emission band at 2.365 eV arises from coupled QDs in the SL, and substructure therein has been attributed to the presence of multiple domains.[1] To directly address this hypothesis, we identified all SLs that show multiple features in the coupled QD emission band: 2-1, 3-2, 3-3, 3-4, 3-5, a subset of which are shown in Figure 4a and the remainder in Figure S2. All of these SLs with the exception of 3-2 exhibit two or more domains at different angles along the angular FFT axis. SL 3-2 shows poor ordering within the STEM image, making domain identification impossible in the majority of the image. We also characterized two SLs that do not obviously exhibit multiple peaks in the PL emission but clearly contain multiple domains in the FFT (2-3, 2-4) (**Figure 4a**, yellow, **S2**). By quantifying the FFT radial peak center and FWHM of both domains, we observe that the two domains in each SL show similar structural properties, which could result in overlapping and indistinguishable PL peaks (**Table S4**). These data suggest that substructure in the red-shifted PL peak does indeed arise from structurally-distinct domains within the SL.

We then correlated the low-temperature PL linewidth to the structural properties obtained from STEM-FFT analysis. In molecular J- and H-aggregates with exciton delocalization, PL linewidth is inversely proportional to the number of coupled emitters, a phenomenon known as exchange narrowing.[44-46] PL linewidths for $CsPbBr_3$ SLs also exhibit exchange narrowing below 100 K commensurate with their degree of coherence, though some convolution with inhomogeneous broadening is present (**Figure S9e**, SI section 4).[3,16] Surveying our population of SLs, we find that PL linewidth has no correlation to FFT linewidth, the primary metric for disorder in the SL assembly (**Figure 4b**). In other words, the extent of exciton delocalization at low-temperature is not dictated by long-range structural order in the SL. We hypothesize that this observation stems from a mismatch in length scales between exciton delocalization and the FFT measurement. The coherent coupling of emitters needed for exciton delocalization occurs over ~3 QDs while STEM-FFT interrogates structural disorder over ~10^5 QDs. Our observations are also consistent with a recent report of superfluorescence in quasi two-dimensional hybrid perovskite films with no long-range structural order.[47] We anticipate that optical phenomenon that occur on longer length scales, for example exciton transport, may be more closely correlated to structural disorder measured by STEM-FFT.[48-51] In contrast to the FWHM, the FFT peak center shows a modest negative correlation with the low-temperature PL linewidth (**Figure 4c**). SLs comprising larger QDs tend to have narrower low-temperature PL peaks and therefore greater exciton coherence relative to SLs with smaller QDs or the polydisperse QD films. We postulate that SLs containing the largest QDs (10-11 nm) exhibit coherence that is more tolerant to size heterogeneity because individual QDs have more similar excited state energies compared to equivalently polydisperse SLs centered around smaller QDs (7-8 nm). The size dependence may also arise in part from the van der Waal's and osmotic interactions that govern the self-assembly process in solution. Stronger associative interactions between larger QDs in the growth solution may cause these SLs to assemble into more strongly-coupled local domains even when significant global disorder remains.[34]

In summary, we have shown that STEM imaging coupled to FFT analysis is a facile method to characterize the structural properties of individual 3D SLs comprising cubic $CsPbBr_3$ QDs. The radial and angular FFT profiles provide information on the average QD center-to-center distance and size dispersity in the SL as well as the number of crystalline domains. Analyzing 40 $CsPbBr_3$ SLs with this method, we find that QDs undergo size-selection during the evaporative growth, yielding SLs that have narrower QD size distribution and larger average QD size than the precursor solution. Direct comparisons can then be made to the low-temperature PL spectra for individual SLs. We show that PL spectra with multiple features at low-temperature correlate to the presence of multiple cubic crystalline domains in the angular FFT profile. We also find that structural disorder at the whole SL level (>10^5 QDs), represented by line broadening in the radial FFT profile, does not correlate directly to the ability for that SL to exhibit superradiance.

Experimental Section

Self-Assembly of 3D Superlattices via Solvent Evaporation

$CsPbBr_3$ quantum dots were synthesized according to a literature procedure, described in detail in the Supporting Information.[52] Superlattices were then self-assembled from the colloidal QD solution through solvent evaporation using a literature method with some modifications.[1] The 3D SLs were prepared on 8 × 6 mm silicon substrates with 90 nm SiO_2 surface layer. To clean the substrate, the silicon substrate was sonicated in acetone, isopropyl alcohol, and water for 5 min per solvent, then placed in a 120 °C oven to dry. Substrates were placed in a Teflon holder in a jar in the glovebox, and a carbon-coated marked Cu TEM grid (01910-F, Ted Pella) was placed on the silicon substrate. Purified QDs were diluted in toluene to 0.125 – 0.5 μM QDs. The actual concentration of QDs was determined from the absorption spectra using a literature molar extinction coefficient.[53] 27 μL of QDs in toluene were deposited on the silicon, and the jar lid was sealed. The toluene was allowed to slowly evaporate (about 3 hr) to form SLs near the edge of the silicon.

Structural Characterization

TEM images were acquired using an FEI Tecnai T20 TEM equipped with a 200 kV LaB_6 filament. HAADF-STEM images were obtained on a FEI Talos F200X S/TEM with a 200 kV X-FEG field-emission source. SEM images were acquired using a Teneo Volumescope at 5.0 kV and 45° tilt angle. Optical images were acquired using an Olympus BX-51 Microscope with tungsten lamp and DP71 CCD camera. UV-Vis data were collected using an Agilent Cary 6000i UV-Vis-NIR Spectrophotometer equipped with a PMT detector. Solution photoluminescence data were collected on a Varian Cary Eclipse Fluorescence spectrophotometer. Powder XRD patterns were obtained using a Panalytical Empyrean Powder X-ray diffractometer using a 5-axis cradle in Bragg-Brentano geometry.

Steady-State Photoluminescence Measurements

Optical measurements were collected prior to STEM imaging since extended exposure to the electron beam during STEM imaging quenches the fluorescence of the superlattices. Steady-state photoluminescence measurements were performed with the same home-built confocal micro-PL setup as described in our recent publication.[16] Briefly, the SLs were excited using a 447 nm picosecond-pulsed diode laser (LDH-P-C-450B, PicoQuant, full width-half maximum ~50 ps, repetition rate 5 MHz). A 40x objective with a numerical aperture (NA) of 0.6 was used in reflection mode to excite and collect sample emission. A monochromator (Andor Technology) and a thermoelectric-cooled charge-coupled device (CCD, Andor Technology) were used to detect sample emission. A fluence of 180 nJ/cm^2 was used to prevent annihilation and other second order effects. The samples were cooled in a closed-cycle optical cryostat (Cryostation s50, Montana Instruments) with a temperature stability <10 mK. Low-temperature data were collected at 7 K.

Fast-Fourier Transform Analysis of STEM Images

STEM images were cropped to include only the SL, as the presence of dead space led to artifacts in the FFT. Then, a fast Fourier transform was performed in Python with the output array being set to 8196 by 8196 pixels. For the angular data, the FFT image was converted from polar coordinates to Cartesian in GIMP (an open-source image editor). Then, a rectangular plot profile was collected in Fiji (an open-source software for processing and analyzing scientific images).[54] The radial width of the profile had minimal effect on the resulting angular profile. There is an artifact that arises in the angular profile of each FFT, a false intensity along the x-y axes. This was removed by subtracting the artifact peak from a sample with no overlap in the FFT spot with the x-y axes. The radial profile was generated by taking ten-degree wedges over all observed spots between 0 and 180 degrees (i.e., two sets of four peaks would be analyzed by taking ten-degree wedges over the four spots between

0 and 180 degrees) with the radial profile plot plugin in Fiji. For each wedge, the exponential background was subtracted, and these subtracted traces were summed together to give the radial profiles.

The radial parameters, FFT center and FWHM, were calculated from four values. The major radial peak was fit in pixel space with a PseudoVoigt function (5 particularly skewed radial profiles were fit with a BigGauss function), from which the fit peak center and FWHM were extracted. These were averaged with the peak centroid and raw FWHM, respectively, to determine the average FFT center and FWHM.

ASSOCIATED CONTENT

Supporting Information

The Supporting Information is available free of charge on the ACS Publications website.
Materials; synthetic and sample preparation methods; experimental details on electron microscopy and optical measurements; additional characterization data on film and superlattice samples (PDF)

AUTHOR INFORMATION

Corresponding Authors

Christina W. Li – Email: christinawli@purdue.edu
Libai Huang – Email: libai-huang@purdue.edu

Notes

The authors declare no competing financial interests.

ACKNOWLEDGMENT

This work was supported by the National Science Foundation through DMR-2004339. Materials characterization was supported in part by the Research Instrumentation Center in the Department of Chemistry at Purdue University. We acknowledge Alexander Flohr and Olivia Wheeler-Williams for their help in collecting PL data.

REFERENCES

(1) Raino, G.; Becker, M. A.; Bodnarchuk, M. I.; Mahrt, R. F.; Kovalenko, M. V.; Stoferle, T. Superfluorescence from lead halide perovskite quantum dot superlattices. *Nature,* **2018**, *563*, 671-675.

(2) Cherniukh, I.; Raino, G.; Stoferle, T.; Burian, M.; Travesset, A.; Naumenko, D.; Amenitsch, H.; Erni, R.; Mahrt, R. F.; Bodnarchuk, M. I.; Kovalenko, M. V. Perovskite-type superlattices from lead halide perovskite nanocubes. *Nature,* **2021**, *593*, 535-542.

(3) Mattiotti, F.; Kuno, M.; Borgonovi, F.; Janko, B.; Celardo, G. L. Thermal Decoherence of Superradiance in Lead Halide Perovskite Nanocrystal Superlattices. *Nano Lett.,* **2020**, *20*, 7382-7388.

(4) Penzo, E.; Loiudice, A.; Barnard, E. S.; Borys, N. J.; Jurow, M. J.; Lorenzon, M.; Rajzbaum, I.; Wong, E. K.; Liu, Y.; Schwartzberg, A. M.; Cabrini, S.; Whitelam, S.; Buonsanti, R.; Weber-Bargioni, A. Long-Range Exciton Diffusion in Two-Dimensional Assemblies of Cesium Lead Bromide Perovskite Nanocrystals. *ACS Nano,* **2020**, *14*, 6999-7007.

(5) Tang, Y. Y.; Poonia, D.; van der Laan, M.; Timmerman, D.; Kinge, S.; Siebbeles, L. D. A.; Schall, P. Electronic Coupling of Highly Ordered Perovskite Nanocrystals in Supercrystals. *ACS Appl. Energy Mater.,* **2022**, *5*, 5415-5422.

(6) Tang, X. T.; Rossi, D.; Cheon, J.; Son, D. H. Effects of Electronic Coupling on Bright and Dark Excitons in a 2D Array of Strongly Confined $CsPbBr_3$ Quantum Dots. *Chem. Mater.,* **2022**, *34*, 7181-7189.

(7) Tong, Y.; Yao, E. P.; Manzi, A.; Bladt, E.; Wang, K.; Doblinger, M.; Bals, S.; Muller-Buschbaum, P.; Urban, A. S.; Polavarapu, L.; Feldmann, J. Spontaneous Self-Assembly of Perovskite Nanocrystals into Electronically Coupled Supercrystals: Toward Filling the Green Gap. *Adv. Mater.,* **2018**, *30*, 1801117.

(8) van der Burgt, J. S.; Geuchies, J. J.; van der Meer, B.; Vanrompay, H.; Zanaga, D.; Zhang, Y.; Albrecht, W.; Petukhov, A. V.; Filion, L.; Bals, S.; Swart, I.; Vanmaekelbergh, D. Cuboidal Supraparticles Self-Assembled from Cubic $CsPbBr_3$ Perovskite Nanocrystals. *J. Phys. Chem. C,* **2018**, *122*, 15706-15712.

(9) Baranov, D.; Toso, S.; Imran, M.; Manna, L. Investigation into the Photoluminescence Red Shift in Cesium Lead Bromide Nanocrystal Superlattices. *J. Phys. Chem. Lett.,* **2019**, *10*, 655-660.

(10) Zhou, C.; Zhong, Y. C.; Dong, H. X.; Zheng, W. H.; Tan, J. Q.; Jie, Q.; Pan, A. L.; Zhang, L.; Xie, W. Cooperative excitonic quantum ensemble in perovskite-assembly superlattice microcavities. *Nat. Commun.,* **2020**, *11*, 329.

(11) Brennan, M. C.; Toso, S.; Pavlovetc, I. M.; Zhukovskyi, M.; Marras, S.; Kuno, M.; Manna, L.; Baranov, D. Superlattices are Greener on the Other Side: How Light Transforms Self-Assembled Mixed Halide Perovskite Nanocrystals. *ACS Energy Lett.,* **2020**, *5*, 1465-1473.

(12) Krieg, F.; Sercel, P. C.; Burian, M.; Andrusiv, H.; Bodnarchuk, M. I.; Stoferle, T.; Mahrt, R. F.; Naumenko, D.; Amenitsch, H.; Raino, G.; Kovalenko, M. V. Monodisperse Long-Chain Sulfobetaine-Capped $CsPbBr_3$ Nanocrystals and Their Superfluorescent Assemblies. *ACS Cent. Sci.,* **2021**, *7*, 135-144.

(13) Liu, J. K.; Zheng, X. P.; Mohammed, O. F.; Bakr, O. M. Self-Assembly and Regrowth of Metal Halide Perovskite Nanocrystals for Optoelectronic Applications. *Acc. Chem. Res.,* **2022**, *55*, 262-274.

(14) Cherniukh, I.; Raino, G.; Sekh, T. V.; Zhu, C. L.; Shynkarenko, Y.; John, R. A.; Kobiyama, E.; Mahrt, R. F.; Stoferle, T.; Erni, R.; Kovalenko, M. V.; Bodnarchuk, M. I. Shape-Directed Co-Assembly of Lead Halide Perovskite Nanocubes with Dielectric Nanodisks into Binary Nanocrystal Superlattices. *ACS Nano,* **2021**, *15*, 16488-16500.

(15) Cherniukh, I.; Sekh, T. V.; Raino, G.; Ashton, O. J.; Burian, M.; Travesset, A.; Athanasiou, M.; Manoli, A.; John, R. A.; Svyrydenko, M.; Morad, V.; Shynkarenko, Y.; Montanarella, F.; Naumenko, D.; Amenitsch, H.; Itskos, G.; Mahrt, R. F.; Stoferle, T.; Erni, R.; Kovalenko, M. V.; Bodnarchuk, M. I. Structural Diversity in Multicomponent Nanocrystal Superlattices Comprising Lead Halide Perovskite Nanocubes. *ACS Nano,* **2022**, *16*, 7210-7232.

(16) Blach, D. D.; Lumsargis, V. A.; Clark, D. E.; Chuang, C.; Wang, K.; Dou, L.; Schaller, R. D.; Cao, J.; Li, C. W.; Huang, L. Superradiance and Exciton Delocalization in Perovskite Quantum Dot Superlattices. *Nano Lett.,* **2022**, *22*, 7811-7818.

(17) Spano, F. C.; Kuklinski, J. R.; Mukamel, S. Temperature-Dependent Superradiant Decay of Excitons in Small Aggregates. *Phys. Rev. Lett.,* **1990**, *65*, 211-214.

(18) Toso, S.; Baranov, D.; Giannini, C.; Marras, S.; Manna, L. Wide-Angle X-ray Diffraction Evidence of Structural Coherence in $CsPbBr_3$ Nanocrystal Superlattices. *ACS Mater. Lett.,* **2019**, *1*, 272-276.

(19) Huang, H.; Feil, M. W.; Fuchs, S.; Debnath, T.; Richter, A. F.; Tong, Y.; Wu, L. Z.; Wang, Y. O.; Doblinger, M.; Nickel, B. Growth of Perovskite $CsPbBr_3$ Nanocrystals and Their Formed Superstructures Revealed by In Situ Spectroscopy. *Chem. Mater.,* **2020**, *32*, 8877-8884.

(20) Toso, S.; Baranov, D.; Altamura, D.; Scattarella, F.; Dahl, J.; Wang, X. Z.; Marras, S.; Alivisatos, A. P.; Singer, A.; Giannini, C.; Manna, L. Multilayer Diffraction Reveals That Colloidal Superlattices Approach the Structural Perfection of Single Crystals. *ACS Nano,* **2021**, *15*, 6243-6256.

(21) Bertolotti, F.; Vivani, A.; Ferri, F.; Anzini, P.; Cervellino, A.; Bodnarchuk, M. I.; Nedelcu, G.; Bernasconi, C.; Kovalenko, M. V.; Masciocchi, N.; Guagliardi, A. Size Segregation and Atomic Structural Coherence in Spontaneous Assemblies of Colloidal Cesium Lead Halide Nanocrystals. *Chem. Mater.,* **2022**, *34*, 594-608.

(22) Lapkin, D.; Kirsch, C.; Hiller, J.; Andrienko, D.; Assalauova, D.; Braun, K.; Carnis, J.; Kim, Y. Y.; Mandal, M.; Maier, A.; Meixner, A. J.; Mukharamova, N.; Scheele, M.; Schreiber, F.; Sprung, M.; Wahl, J.; Westendorf, S.; Zaluzhnyy, I. A.; Vartanyants, I. A. Spatially resolved fluorescence of caesium lead halide perovskite supercrystals reveals quasi-atomic behavior of nanocrystals. *Nat. Commun.,* **2022**, *13*, 892.

(23) Higgins, R. J. Fast Fourier-Transform - Introduction with Some Minicomputer Experiments. *Am. J. Phys.,* **1976**, *44*, 766-773.

(24) Ou, Z. H.; Wang, Z. W.; Luo, B. B.; Luijten, E.; Chen, Q. Kinetic pathways of crystallization at the nanoscale. *Nat. Mater.,* **2020**, *19*, 450-455.

(25) Ou, Z. H.; Yao, L. H.; An, H.; Shen, B. N.; Chen, Q. Imaging how thermal capillary waves and anisotropic interfacial stiffness shape nanoparticle supracrystals. *Nat. Commun.,* **2020**, *11*, 4555.

(26) Lee, Y. H.; Lay, C. L.; Shi, W. X.; Lee, H. K.; Yang, Y. J.; Li, S. Z.; Ling, X. Y. Creating two self-assembly micro-environments to achieve supercrystals with dual structures using polyhedral nanoparticles. *Nat. Commun.,* **2018**, *9*, 2769.

(27) Bergstrom, L.; Sturm, E. V.; Salazar-Alvarez, G.; Colfen, H. Mesocrystals in Biominerals and Colloidal Arrays. *Acc. Chem. Res.,* **2015**, *48*, 1391-1402.

(28) Deng, K. R.; Luo, Z. S.; Tan, L.; Quan, Z. W. Self-assembly of anisotropic nanoparticles into functional superstructures. *Chem. Soc. Rev.,* **2020**, *49*, 6002-6038.

(29) Auyeung, E.; Li, T. I. N. G.; Senesi, A. J.; Schmucker, A. L.; Pals, B. C.; de la Cruz, M. O.; Mirkin, C. A. DNA-mediated nanoparticle crystallization into Wulff polyhedra. *Nature,* **2014**, *505*, 73-77.

(30) Baranov, D.; Fiore, A.; van Huis, M.; Giannini, C.; Falqui, A.; Lafont, U.; Zandbergen, H.; Zanella, M.; Cingolani, R.; Manna, L. Assembly of Colloidal Semiconductor Nanorods in Solution by Depletion Attraction. *Nano Lett.,* **2010**, *10*, 743-749.

(31) Glotzer, S. C.; Solomon, M. J. Anisotropy of building blocks and their assembly into complex structures. *Nat. Mater.,* **2007**, *6*, 557-562.

(32) Lv, Z. P.; Kapuscinski, M.; Bergstrom, L. Tunable assembly of truncated nanocubes by evaporation-driven poor-solvent enrichment. *Nat. Commun.,* **2019**, *10*, 4228.

(33) Nakagawa, F.; Saruyama, M.; Takahata, R.; Sato, R.; Matsumoto, K.; Teranishi, T. In Situ Control of Crystallinity of 3D Colloidal Crystals by Tuning the Growth Kinetics of Nanoparticle Building Blocks. *J. Am. Chem. Soc.,* **2022**, *144*, 5871-5877.

(34) Lokteva, I.; Dartsch, M.; Dallari, F.; Westermeier, F.; Walther, M.; Grubel, G.; Lehmkuhler, F. Real-Time X-ray Scattering Discovers Rich Phase Behavior in PbS Nanocrystal Superlattices during In Situ Assembly. *Chem. Mater.,* **2021**, *33*, 6553-6563.

(35) Ondry, J. C.; Frechette, L. B.; Geissler, P. L.; Alivisatos, A. P. Trade-offs between Translational and Orientational Order in 2D Superlattices of Polygonal Nanocrystals with Differing Edge Count. *Nano Lett.,* **2022**, *22*, 389-395.

(36) Kapuscinski, M.; Agthe, M.; Lv, Z. P.; Liu, Y. X.; Segad, M.; Bergstrom, L. Temporal Evolution of Superlattice Contraction and Defect-Induced Strain Anisotropy in Mesocrystals during Nanocube Self-Assembly. *ACS Nano,* **2020**, *14*, 5337-5347.

(37) Weidman, M. C.; Smilgies, D. M.; Tisdale, W. A. Kinetics of the self-assembly of nanocrystal superlattices measured by real-time in situ X-ray scattering. *Nat. Mater.,* **2016**, *15*, 775-781.

(38) Agthe, M.; Wetterskog, E.; Bergstrom, L. Following the Assembly of Iron Oxide Nanocubes by Video Microscopy and Quartz Crystal Microbalance with Dissipation Monitoring. *Langmuir,* **2017**, *33*, 303-310.

(39) Goubet, N.; Portales, H.; Yan, C.; Arfaoui, I.; Albouy, P. A.; Mermet, A.; Pileni, M. P. Simultaneous Growths of Gold Colloidal Crystals. *J. Am. Chem. Soc.,* **2012**, *134*, 3714-3719.

(40) Rupich, S. M.; Shevchenko, E. V.; Bodnarchuk, M. I.; Lee, B.; Talapin, D. V. Size-Dependent Multiple Twinning in Nanocrystal Superlattices. *J. Am. Chem. Soc.,* **2010**, *132*, 289-296.

(41) Pronk, S.; Frenkel, D. Large effect of polydispersity on defect concentrations in colloidal crystals. *J. Chem. Phys.,* **2004**, *120*, 6764-6768.

(42) Auer, S.; Frenkel, D. Suppression of crystal nucleation in polydisperse colloids due to increase of the surface free energy. *Nature,* **2001**, *413*, 711-713.

(43) Zaitseva, N.; Dai, Z. R.; Leon, F. R.; Krol, D. Optical properties of CdSe superlattices. *J. Am. Chem. Soc.,* **2005**, *127*, 10221-10226.

(44) Spano, F. C.; Mukamel, S. Superradiance in Molecular Aggregates. *J. Chem. Phys.,* **1989**, *91*, 683-700.

(45) Potma, E. O.; Wiersma, D. A. Exciton superradiance in aggregates: The effect of disorder, higher order exciton-phonon coupling and dimensionality. *J. Chem. Phys.,* **1998**, *108*, 4894-4903.

(46) Meinardi, F.; Cerminara, M.; Sassella, A.; Bonifacio, R.; Tubino, R. Superradiance in molecular H aggregates. *Phys. Rev. Lett.,* **2003**, *91*, 247401.

(47) Biliroglu, M.; Findik, G.; Mendes, J.; Seyitliyev, D.; Lei, L.; Dong, Q.; Mehta, Y.; Temnov, V. V.; So, F.; Gundogdu, K. Room-temperature superfluorescence in hybrid perovskites and its origins. *Nat. Photonics,* **2022**, *16*, 324-329.

(48) Bardeen, C. J. The Structure and Dynamics of Molecular Excitons. *Annu. Rev. Phys. Chem.,* **2014**, *65*, 127-148.

(49) Ahn, T. S.; Wright, N.; Bardeen, C. J. The effects of orientational and energetic disorder on Forster energy migration along a one-dimensional lattice. *Chem. Phys. Lett.,* **2007**, *446*, 43-48.

(50) Schonherr, G.; Eiermann, R.; Bassler, H.; Silver, M. Dispersive Exciton Transport in a Hopping System with Gaussian Energy-Distribution. *Chem. Phys.,* **1980**, *52*, 287-298.

(51) Athanasopoulos, S.; Emelianova, E. V.; Walker, A. B.; Beljonne, D. Exciton diffusion in energetically disordered organic materials. *Phys. Rev. B,* **2009**, *80*, 195209.

(52) Protesescu, L.; Yakunin, S.; Bodnarchuk, M. I.; Krieg, F.; Caputo, R.; Hendon, C. H.; Yang, R. X.; Walsh, A.; Kovalenko, M. V. Nanocrystals of Cesium Lead Halide Perovskites ($CsPbX_3$, X = Cl, Br, and I): Novel Optoelectronic Materials Showing Bright Emission with Wide Color Gamut. *Nano Lett.,* **2015**, *15*, 3692-3696.

(53) Maes, J.; Balcaen, L.; Drijvers, E.; Zhao, Q.; De Roo, J.; Vantomme, A.; Vanhaecke, F.; Geiregat, P.; Hens, Z. Light Absorption Coefficient of $CsPbBr_3$ Perovskite Nanocrystals. *J. Phys. Chem. Lett.,* **2018**, *9*, 3093-3097.

(54) Schindelin, J.; Arganda-Carreras, I.; Frise, E.; Kaynig, V.; Longair, M.; Pietzsch, T.; Preibisch, S.; Rueden, C.; Saalfeld, S.; Schmid, B.; Tinevez, J. Y.; White, D. J.; Hartenstein, V.; Eliceiri, K.; Tomancak, P.; Cardona, A. Fiji: an open-source platform for biological-image analysis. *Nat. Methods,* **2012**, *9*, 676-682.

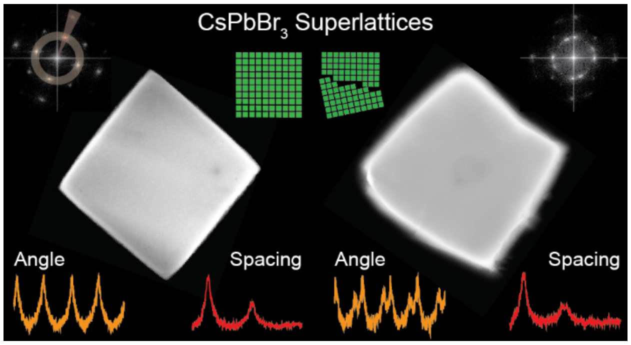

TOC Graphic